Weak ferromagnetism and spin reorientation in antiferroelectric BiCrO₃

Dylan Behr,[1,*] Davide Delmonte [2] Edmondo Gilioli [2] Dmitry D. Khalyavin,[3] and Roger D. Johnson [1]

[1]*Department of Physics and Astronomy, University College London, Gower Street, London WC1E 6BT, United Kingdom*
[2]*IMEM-CNR, Istituto dei Materiali per l'Elettronica e il Magnetismo, Parco Area delle Scienze, 37/A, 43124 Parma, Italy*
[3]*ISIS facility, Rutherford Appleton Laboratory-STFC, Chilton, Didcot OX11 0QX, United Kingdom*

BiCrO₃ is an antiferroelectric perovskite known to exhibit an unconventional spin reorientation transition between antiferromagnetic structures, accompanied by a large jump in weak ferromagnetism. Using a combination of neutron powder diffraction, magnetometry, and symmetry analysis, we confirm the dominant G-type antiferromagnetic order below $T_N = 111$ K and identify the magnetic phase transition with a spontaneous rotation of Cr^{3+} moments from the b axis to a particular direction in the ac plane. We demonstrate the role of antiferroelectric displacements produced by the Bi^{3+} lone-pair electrons and octahedral rotations in establishing spin canting via the antisymmetric Dzyaloshinskii-Moriya interaction. This mechanism results in weak ferromagnetism above and below the spin-reorientation and explains the dramatic increase in net magnetization on cooling.

I. INTRODUCTION

Spontaneous spin-reorientation (SR) transitions are characterized by a cooperative rotation of spins on a magnetically ordered sublattice. Such phenomena have attracted substantial attention from the condensed matter and materials physics community, both for their implications for the fundamental nature of magnetic order and dynamics [1] and for wider technological applications: SR transitions may play a vital role in spintronic devices used for novel memory storage and manipulation in next generation computing [2,3]. Indeed, the ability to switch (staggered) magnetization from one regime to another at high frequency is an essential characteristic for the realization of competitive magnetic random access memory [4,5].

Orthoferrite perovskites of the form REFeO₃ (where RE denotes a rare earth element) demonstrate canonical SR phenomena. In these systems, the perovskite B-site transition metal sublattice hosts an antiferromagnetic (AFM) staggered magnetization at all temperatures below T_N [6]. For compounds with a magnetic RE ion on the perovskite A-site, a f-d exchange interaction couples the magnetic order on the RE sublattice to that on the Fe sublattice. If the RE sublattice has a different anisotropy to that of the Fe sublattice, then they compete for a preferred orientation of spins resulting in the observed SR transitions [7]. A similar mechanism of SR has recently been reported in an orthoferrite system with nonmagnetic A-site cations: In PbFeO₃, Pb^{2+}:Pb^{4+} charge ordering and the respective accommodation of Pb^{2+} lone-pair electrons leads to large, symmetry breaking structural distortions that split the Fe sites into two symmetry-inequivalent sublattices with different magnetic anisotropies [8]. The relative amplitude of the structural distortions favoring each anisotropy was found to have a significant temperature dependence, giving rise to a high temperature SR transition [8]. While

coexisting magnetic sublattices with competing anisotropies naturally lead to SR, the perovksite-type structural framework has been found to host SR phenomena beyond this paradigm. For example, in the columnar ordered quadruple perovskites Y₂CuMnMn₄O₁₂ and Dy₂CuMnMn₄O₁₂ multiple SR transitions occur due to an instability towards AFM spin canting combined with Dzyaloshinskii-Moriya (DM) and single-ion anisotropies [9].

The perovskite BiCrO₃ (BCO) is known to exhibit a SR transition at low temperature [10], however there is little consensus on the underlying mechanism and the exact magnetic structure above and below the transition temperature. BCO adopts a monoclinic ($C2/c$) crystal structure below 410 K, which can be considered a superstructure of the $Pm\bar{3}m$ simple perovskite where $\mathbf{a} = [2, 1, 1]_c$, $\mathbf{b} = [0, 1, -1]_c$ and $\mathbf{c} = [-2, 1, 1]_c$ (each lattice vector is defined in the basis of the $Pm\bar{3}m$ cubic (c) perovskite unit cell, see Appendix A). The formation of this superstructure can be understood in terms of an antiferroelectric ordering of the Bi^{3+} lone-pair electrons, which, similar to the case of PbFeO₃, splits the Cr^{3+} sites into two symmetry inequivalent sublattices. An early study indicated parasitic ferromagnetism below 114 K [11], which has since been identified as a phase transition to G-type antiferromagnetic order of the Cr^{3+} ions with a weak ferromagnetic moment through spin canting [12]. A dramatic rise in magnetic susceptibility was observed below $T_{SR} \sim 80$ K, which was reported to be accompanied by a global reorientation of spins by $\sim 50°$ from the monoclinic b axis towards the c axis [10]. However, the precise nature of this low temperature phase could not be elucidated, including the enhanced magnetization and underlying SR mechanism. It was later pointed out that this low temperature magnetic model was inconsistent with group theory, and a scenario in which the SR transition involved a rotation of moments confined to the ac plane was proposed instead [13,14]. Furthermore, recent Raman scattering measurements have suggested a significant role of magnetostructural coupling in this complex phase diagram [15].
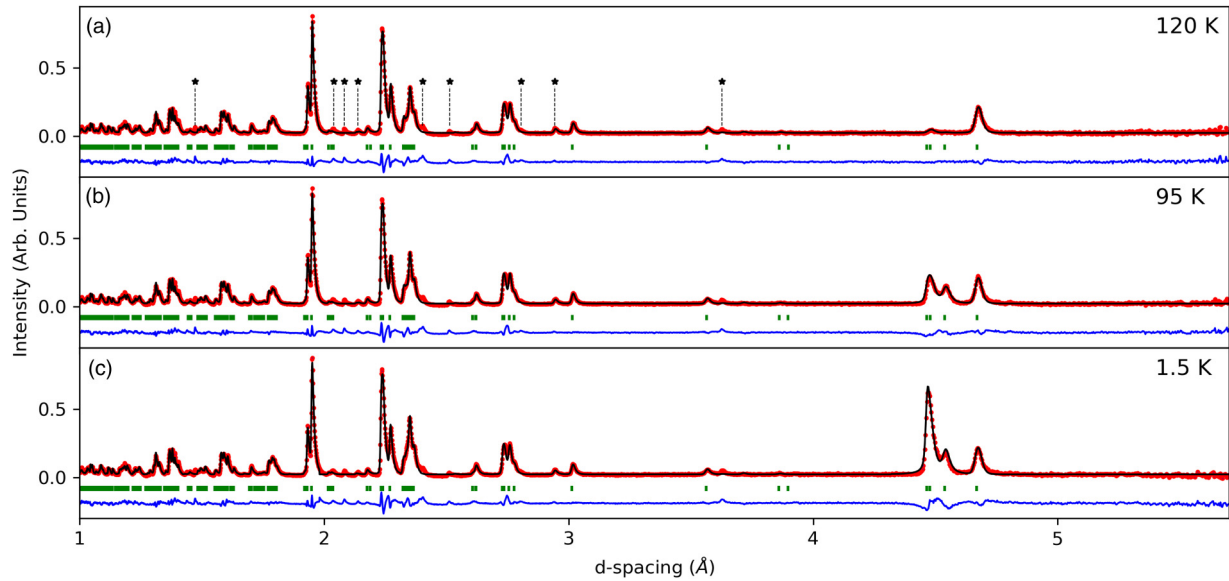
*dylan.behr.20@ucl.ac.uk

FIG. 1. Neutron powder diffraction data (red circles) measured at (a) 120 K in the paramagnetic phase (b) 95 K in the high temperature magnetic ordered phase (c) 1.5 K in the low temperature magnetic ordered phase. Fits to the data are shown as black lines, nuclear and magnetic peak positions are indicated by green tick marks, and the difference $I_{\text{obs}} - I_{\text{calc}}$ is shown in blue. Impurity peaks are indicated with small black stars on the 120 K spectrum.

Taking into account these results, we reinvestigate the magnetic structure of BCO and its temperature evolution through analysis of high-resolution neutron powder diffraction (NPD) data. In line with previous reports [16], we demonstrate that BCO adopts an approximately collinear G-type AFM structure at all temperatures below $T_N = 110$ K. However, contrary to the above, we show that at $T_{SR} \sim 75$ K the magnetic moments globally rotate from the monoclinic b axis into the ac plane parallel to $[1, 0, -1]$. This transition is translated to higher temperatures in an applied DC field. The magnetic structures above and below T_{SR} transform by different, single irreducible representations (irreps) of the monoclinic paramagnetic parent, implying a first-order SR transition, as observed. We derive free energy invariants that couple displacive modes associated with CrO_6 octahedral tilts and Bi^{3+} antiferroelectric distortions to the spin degrees of freedom. This approach provides a useful insight into the nature of weak ferromagnetism and naturally explains the dramatic change in the net magnetization at the SR transition.

The paper is organized as follows. We first present the experimental details in Sec. II. The paramagnetic crystal structure refined against NPD is presented in Sec. III A, DC magnetometry measurements are discussed in Sec. III B, and the magnetic structures are reported in Sec. III C. In an extended discussion (Sec. IV), we introduce a symmetry-based approach to understand the origin of weak ferromagnetism, briefly discuss the SR transition and present the field dependence of the magnetic transitions. Finally, we summarize our conclusions in Sec. V.

II. EXPERIMENT

A polycrystalline sample of $BiCrO_3$ in the form of a fine powder was synthesized under high pressure, high temperature conditions from stoichiometric mixtures of Bi_2O_3

and Cr_2O_3 starting reagents as detailed in Refs. [14,17]. Neutron powder diffraction experiments were performed using the time-of-flight diffractometer WISH at ISIS [18]. An 80-mg sample was loaded into a cylindrical 3-mm-diameter vanadium can and cooled to a base temperature of 1.5 K. Diffraction data with good counting statistics (30 min per measurement) were collected on warming from 1.5 up to 80 K in 10 K steps and on up to 120 K in 5 K steps. Measurements with high counting statistics (2–3 h per measurement) were made in the paramagnetic phase at 120 K and in the high and low temperature magnetic phases at 95 and 1.5 K, respectively. Rietveld refinements of the crystal structure were performed using FULLPROF [19] while symmetry analyses were performed using the ISOTROPY software suite [20], including the ISODISTORT tool [21]. Initial magnetometry measurements were performed on a vibrating sample magnetometer (Quantum Design PPMS-VSM) between 2 K and 300 K in 100 Oe and 500 Oe fields under both zero-field-cooled (ZFC) and field-cooled-on-cooling (FCC) conditions. Isothermal magnetization measurements were performed between −80 and 80 kOe at 2 and 100 K. Additional magnetometry measurements were performed on a SQUID magnetometer (Quantum Design MPMS-3) between 40 and 200 K under FCC and field-cooled-on-warming (FCW) conditions. One further ZFC measurement between 40 and 400 K was performed at 1 T to extract Curie-Weiss behavior.

III. RESULTS

A. Crystal structure

A structural model based upon the published $C2/c$ crystal structure of BCO [14] was refined against NPD data measured in the paramagnetic phase at 120 K (Fig. 1). Lattice parameters refined to $a = 9.4520(4)$ Å, $b = 5.4749(2)$ Å, $c = 9.5783(3)$ Å and $\beta = 108.562(3)°$, in

TABLE I. $C2/c$ crystal structure parameters of BiCrO$_3$ refined at 120, 95, and 1.5 K. Atomic Wyckoff positions are as follows. Bi: $8f[x, y, z]$, Cr1: $4e[0, y, \frac{1}{4}]$, Cr2: $4d[\frac{1}{4}, \frac{1}{4}, \frac{1}{2}]$, O1, O2 & O3: $8f[x, y, z]$. B_{iso} is given in units of Å^2.

T (K)		120	95	1.5
Lattice parameters				
a (Å)		9.4520(4)	9.4516(4)	9.4500(4)
b (Å)		5.4749(2)	5.4741(2)	5.4729(2)
c (Å)		9.5783(3)	9.5765(3)	9.5747(3)
β (°)		108.562(3)	108.561(3)	108.560(3)
Fractional coordinates and a.d.p.s				
Bi	x	0.1345(4)	0.1343(4)	0.1335(4)
	y	0.2068(8)	0.2079(7)	0.2083(7)
	z	0.1276(6)	0.1273(5)	0.1264(6)
	B_{iso}	1.7(1)	1.2(1)	1.2(1)
Cr1	y	0.224(2)	0.226(2)	0.226(2)
	B_{iso}	0.8(3)	0.6(3)	0.6(3)
Cr2	B_{iso}	1.0(3)	1.0(3)	0.8(3)
O1	x	0.0849(5)	0.0851(5)	0.0856(6)
	y	0.214(1)	0.214(1)	0.215(1)
	z	0.5865(5)	0.5856(5)	0.5863(6)
	B_{iso}	1.7(2)	1.9(1)	2.0(1)
O2	x	0.1569(7)	0.1568(7)	0.1574(7)
	y	0.528(2)	0.528(1)	0.529(1)
	z	0.3637(7)	0.3640(7)	0.3650(7)
	B_{iso}	2.5(2)	2.1(2)	2.0(2)
O3	x	0.3574(7)	0.3581(8)	0.3580(8)
	y	0.523(1)	0.524(1)	0.524(1)
	z	0.1574(6)	0.1581(7)	0.1575(7)
	B_{iso}	2.6(2)	2.6(2)	2.4(2)
Reliability parameters				
R (%)		3.35	3.00	3.31
wR (%)		4.69	4.34	4.48

good agreement with the results reported in Refs. [10,13,14]. Asymmetric peak broadening was observed in the diffraction spectra that we suggest originates in a strain associated with inhomogeneous antiferroelectric displacements. Such static disorder is reflected in the anomalously high isotropic displacement values obtained for bismuth and oxygen ions at low temperature. Despite this peak broadening, reasonable goodness-of-fit parameters of $R_{Bragg} = 8.60\%$, $R = 3.35\%$ and $wR = 4.69\%$ were achieved, and the refined structural parameters (Table I) were used as a reference in the refinement of the magnetic phases described below. We note that the magnetic Cr ions are split into two symmetry inequivalent sublattices at Wyckoff positions $4e$ and $4d$.

A number of weak reflections were not accounted for by the above model, but were instead identified as arising from vanadium (sample can) and small amounts of Bi$_2$(CO$_3$)O$_2$ (1.00 wt%) and Cr$_2$O$_3$ (0.65 wt%) impurity phases. A significant further impurity remained unidentified.

B. Magnetometry

Both ZFC and FCC dc magnetic susceptibilities of our BCO sample [Fig. 2(a)] were found to be qualitatively consistent with previous reports [13,22]. Below $T_N = 111$ K
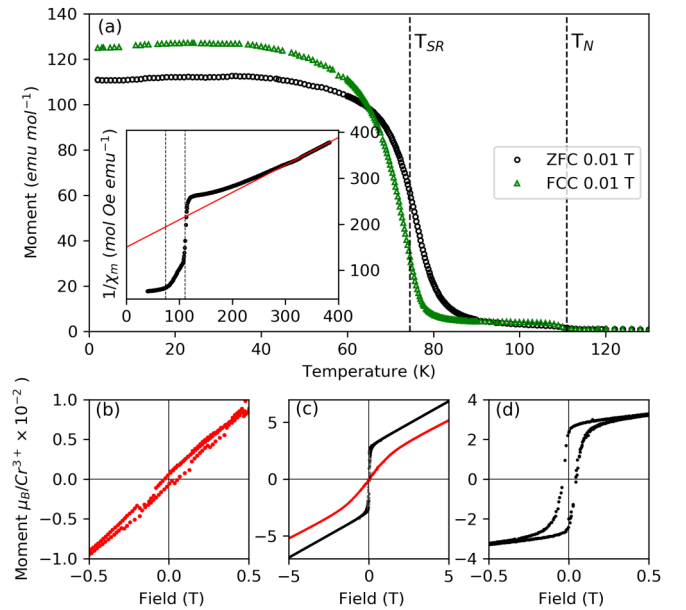

FIG. 2. (a) ZFC and FCC magnetization measurements of the BCO sample under an applied DC field of 100 Oe. The inset shows the inverse molar susceptibility, χ_m, calculated from the magnetization measured in a DC field of 1 T. The bottom row (b)–(d) show magnetization as a function of applied field H taken at temperatures 100 K (b), (c): red and 2 K (d), (c): black. The linear response of magnetization exhibited for high fields continues beyond 5 T up until the maximum measured field of 8 T.

the bulk magnetization shows an anomalous increase indicative of a phase transition to a long-range ordered magnetic structure with a weak, net ferromagnetic moment. On further cooling below $T_{SR} = 75$ K the magnetic susceptibility shows a dramatic increase, consistent with a second phase transition to a ground state magnetic structure with a larger weak ferromagnetic moment. The presence of thermal hysteresis ($T_{SR} = 75.9$ K and 73.7 K for the data sets measured on warming and cooling, respectively) demonstrates that this transition is strongly first order.

At high temperatures there exists a significant departure from Curie-Weiss (CW) behavior between $T_N < T < 250$ K [see Fig. 2(a), inset], indicating the presence of strong short-range correlations well above the onset of magnetic order. CW fitting of the inverse susceptibility in a 1 T applied field in the temperature range $350 < T < 400$ K allowed us to extract an effective moment of 3.67 μ_B/Cr^{3+}, in line with the theoretical effective moment of 3.87 μ_B for a $S = \frac{3}{2}$, 3d^3 Cr^{3+} ion. The same fit gives a Curie-Weiss temperature of $\theta_C = -253$ K, consistent with strong antiferromagnetic interactions.

The presence of weak ferromagnetism in the magnetically ordered phases of BCO is confirmed via measurements of magnetization as a function of applied magnetic field [Figs. 2(b)–2(d)]. Data collected at 100 and 2 K both show ferromagnetic hysteresis at low fields with a small coercive field of approximately 240 Oe and 430 Oe, respectively. The powder averaged remnant magnetization of these phases is approximately $6 \times 10^{-4} \mu_B$ and $2.3 \times 10^{-2} \mu_B$, implying an order of magnitude increase in the weak ferromagnetic

moment consistent with FCC and ZFC dc susceptibility measurements.

C. Magnetic structures

Concomitant with changes in the magnetometry data, we observed changes in the neutron powder diffraction data as temperature was decreased. Below $T_N = 111$ K magnetic peaks appeared that could be indexed $\{\bar{1}11\}$, $\{200\}$ and $\{002\}$ with respect to the $C2/c$ crystal structure [see Fig. 3(a)]; consistent with the onset of long-range magnetic order at the Γ-point; $\mathbf{k} = (0, 0, 0)$. Assuming a second-order phase transition at T_N, symmetry analysis using ISODISTORT combined with structure factor calculations revealed just two collinear antiferromagnetic candidate structures for the intermediate magnetic phase ($T_{SR} < T < T_N$). Both structures comprised ferromagnetic Cr1 and Cr2 sublattices antialigned with one another, i.e., a G-type antiferromagnetic structure with characteristic reflection conditions $h0l$: $h, l = 2n$ and $h - l = 4n - 2$. One candidate had the G-type staggered magnetization lying parallel to the monoclinic b axis, and the other in the ac plane (see Fig. 4). The respective magnetic space groups (MSG) were $C2/c$ (transforming as the $m\Gamma_1^+$ irrep) and $C2'/c'$ (transforming as $m\Gamma_2^+$ irrep). Rietveld refinements against neutron powder diffraction data measured at 95 K revealed that both candidate structures could reasonably fit the observed diffraction data. Yet, as shown in Figs. 3(b) and 3(c), we were able to unambiguously determine that the 95 K structure has moments lying parallel to the monoclinic b axis, transforming as $m\Gamma_1^+$ (MSG $C2/c$); see Figs. 4(a) and 4(b) and .mcif file in the Supplemental Material [23]. As is typically the case, we note that the NPD refinements were not sensitive to subtle spin canting or small differences in moment magnitudes on the Cr1 and Cr2 sites. Thus, in order to stabilize refinements and reduce correlation with the nuclear structure, Cr1 and Cr2 sublattices were constrained to be collinear and host magnetic moments of equal magnitude, which freely refined to 1.81 μ_B/Cr^{3+} site at this temperature.

As shown in Fig. 3(a), the $\{\bar{1}11\}$ family of reflections grew significantly on cooling below $T_{SR} = 75$ K, while the intensity of the $\{200\}$ and $\{002\}$ peaks remained approximately the same. Rietveld refinements were performed against neutron powder diffraction data measured at 1.5 K. Unlike the 95 K magnetic phase, the low temperature diffraction data could only be fitted by a MSG $C2'/c'$ magnetic structure model transforming by $m\Gamma_2^+$. In this symmetry, Cr^{3+} moments are free to rotate in the ac plane and they refined to lie along $[1, 0, -1]$ to within 16°; approximately parallel to a local O-Cr-O axis of each CrO$_6$ octahedron[see Figs. 4(c) and 4(d) and .mcif file [23]). As above the refinement was not sensitive to any symmetry allowed spin canting. The magnetic moment on each Cr^{3+} site freely refined to 2.82 μ_B at this temperature, in good agreement with the 3μ_B moment expected for the [Ar]3d^3 $S = 3/2$ ground state electronic configuration.

The above magnetic structure models were systematically refined against neutron powder diffraction data measured as a function of temperature. Figure 5(a) shows the temperature dependence of the magnetic moments. At T_N these values were well fit with the functional form $m(T) = m_0(1 - (T/T_N)^\alpha)^\beta$ arising from the interpolation of the Bloch law
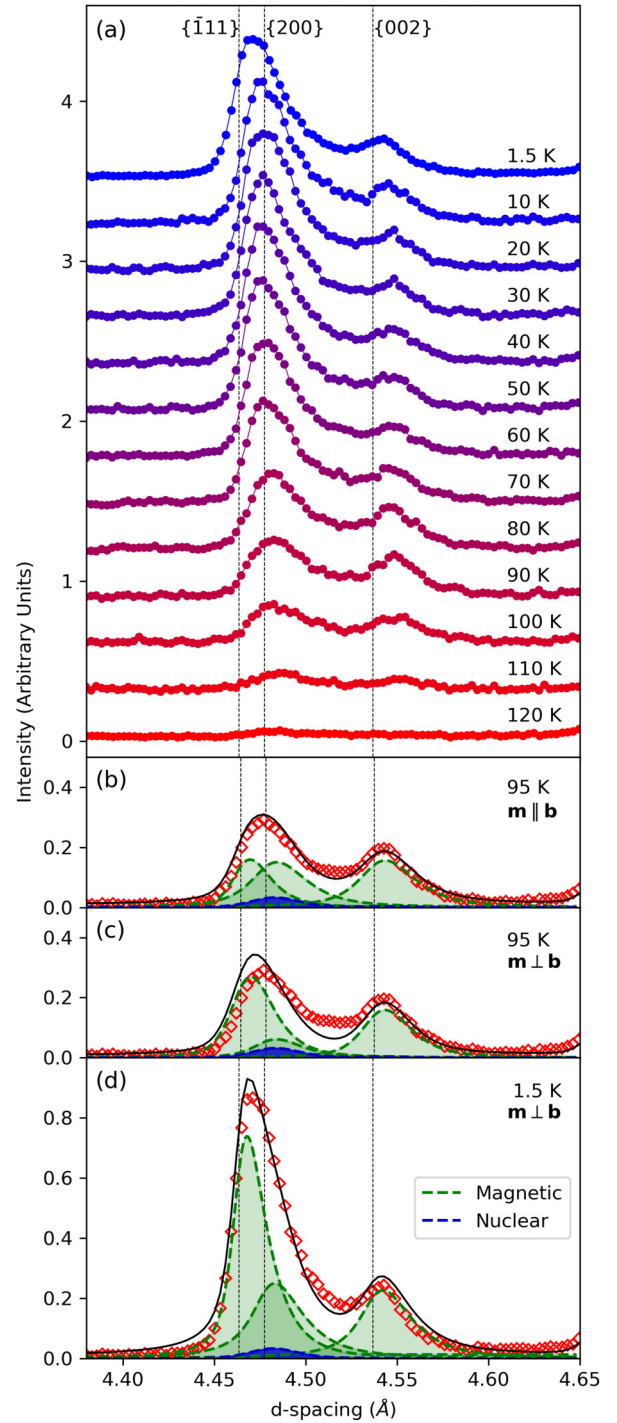

FIG. 3. (a) Thermal evolution of the $\{\bar{1}11\}$, $\{200\}$, and $\{002\}$ magnetic peaks. (b) 95 K magnetic structure model refinements under $m\Gamma_1^+$ constraints and (c) under $m\Gamma_2^+$ constraints. d) 1.5 K magnetic structure model refined under $m\Gamma_2^+$ constraints.

for ferromagnets [24] and critical behavior [25], with a least-squares optimization converging to values of $m_0 = 2.71\mu_B$, $T_N = 113.4$ K, $\alpha = 2.80$ and $\beta = 0.40$. The first-order nature of the spin reorientation transition implies a region of phase coexistence between both magnetic phases, as presented in Fig. 5(b). This model gives a 50:50 phase ratio at ~73.5 K,
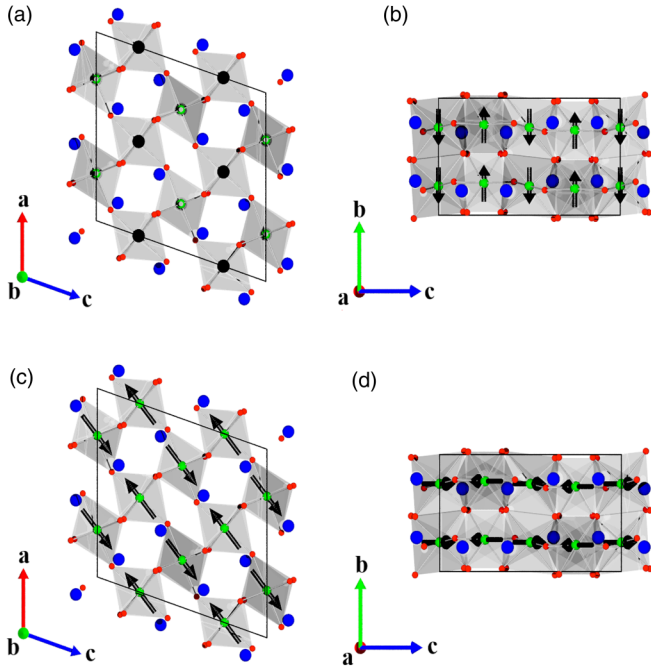
FIG. 4. Magnetic structure at 95 K (a), (b) and 1.5 K (c), (d), transforming as $m\Gamma_1^+$ and $m\Gamma_2^+$, respectively. Magnetic moments (black arrows) lie along **b** at 95 K and in the *ac* plane at 1.5 K. Bismuth, blue spheres; chromium, green spheres; and oxygen, red spheres. CrO_6 octahedra are shaded in grey.

FIG. 6. Type I (a), (b) and Type II (c), (d) canting schemes, transforming as $m\Gamma_1^+$ and $m\Gamma_2^+$, respectively. Canting is exaggerated for clarity and not intended to reflect the true structures. Magnetic moments of on Cr1 and Cr2 sublattices are represented in light and dark green, respectively. Bi and O atoms have been removed for simplicity.
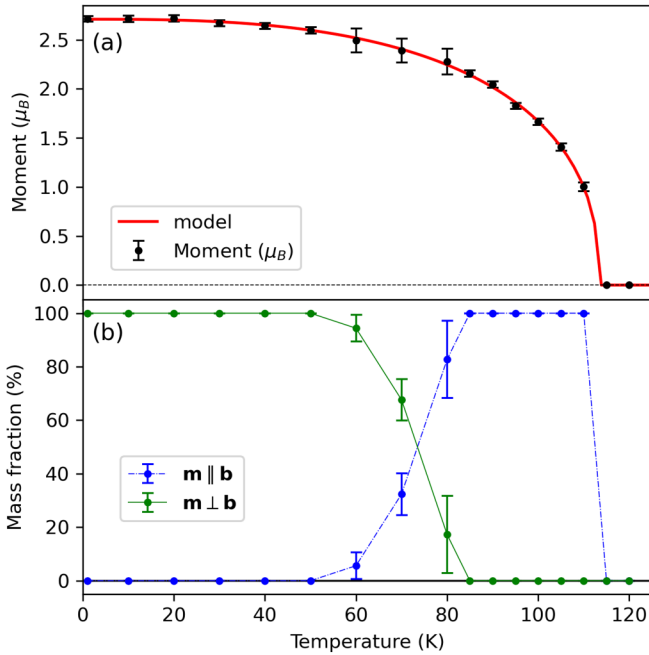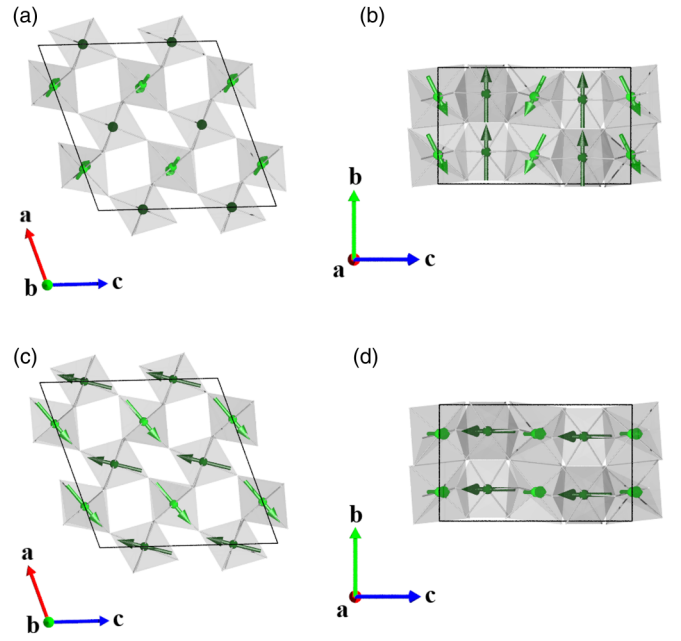

FIG. 5. (a) Temperature dependence of Cr^{3+} moment magnitudes with a Bloch law/critical behavior model fitted to the data (red). (b) Thermal dependence of the mass fraction of magnetic phases transforming as $m\Gamma_1^+$ (blue) and $m\Gamma_2^+$ (green) through the SR transition. Model refinements performed in the temperature ranges $T \leqslant 50$ K and $85 \leqslant T \leqslant 110$ K are constrained to a single magnetic phase, hence mass fraction standard errors are zero, and moment magnitude standard errors are significantly reduced.

in good agreement with the transition temperature of 75 K extracted from magnetometry measurements.

IV. DISCUSSION

The magnetic space groups $C2/c$ ($m\Gamma_1^+$) and $C2'/c'$ ($m\Gamma_2^+$), found above and below T_{SR}, respectively, allow for weak ferromagnetism induced by different schemes of spin canting. We define two canting schemes as type I and type II: Type I canting ($T > T_{SR}$) involves the linear superposition of secondary *antiferromagnetic* modes L_x and L_z (subscripts indicate directions in the right-handed orthonormal basis system with $\mathbf{x} \parallel \mathbf{a}_m$, $\mathbf{y} \parallel \mathbf{b}_m$ and $\mathbf{z} \parallel \mathbf{c^*}_m$, see Appendix C for definitions of all magnetic modes) with spin components perpendicular to the primary G_y mode and localized on the Cr2 sublattice only (Wyckoff position $4d$, site symmetry $\bar{1}$). Moments on Cr2 sites in the same *ab* plane cant in the same direction, while those adjacent along **c*** cant in the opposite sense [see Figs. 6(a) and 6(b)]. In this case weak ferromagnetism (F_y) parallel to the *b* axis emerges due to a net reduction in the *b* axis spin components of the canted Cr2 ions, which no longer exactly cancel the Cr1 moments. Assuming Cr1 and Cr2 moments carry the same size moments, the resulting net magnetization is proportional to $1 - \cos(\theta_I) \approx \frac{\theta_I^2}{2}$ where the canting angle between nearest-neighbor Cr1 and Cr2 spins, θ, is assumed to be small. Type II canting ($T < T_{SR}$) involves the linear superposition of secondary *ferromagnetic* modes (F_x, F_z) with spin components polarized in the *ac* plane and perpendicular to the primary (G_x, G_z) modes [Figures 6(c)–6(d)]. By assuming that Cr1 and Cr2 sublattices remain collinear but counter-rotate with respect to each other,

one obtains a net magnetization proportional to $\sin(\frac{\theta_{II}}{2}) \approx \frac{\theta_{II}}{2}$. We note that additional spin canting is allowed in MSG $C2'/c'$ corresponding to the superposition of a L_y mode on the Cr2 sites, which resembles the type I canting scheme.

If the SR involves a transition between type I and type II canting schemes one can expect a $\frac{\sin(\theta_{II}/2)}{1-\cos(\theta_I)} \approx \frac{\theta_{II}}{\theta_I^2}$-fold increase in net moment on cooling through the transition. By estimating the weak ferromagnetic moment above and below T_{SR} from M vs H measurements (see Fig. 2), we find $\theta_I \sim \theta_{II} \sim 3°$ in both phases. We note that the similar canting angles above and below T_{SR} points towards the same microscopic interactions being active. We explore this in the following.

It is well known that weak ferromagnetism is a coupling phenomenon caused by antisymmetric exchange activated by structural distortions. In the original approach by Dzyaloshinskii [26], the coupling between primary AFM and secondary ferromagnetic order parameters is described by bilinear free energy terms, invariant with respect to the paramagnetic space group. In this approach, however, it is not always clear which distortions are responsible for the coupling nor which components of the magnetic structure are coupled. This drawback can be overcome if instead of the paramagnetic space group, a higher symmetry parent is used where the relevant magnetic modes are decoupled [27,28]. In this case, the appropriate structural distortion must be included to form a free energy invariant.

In discussing the coupling phenomena in perovskite structures, it is convenient to use the cubic $Pm\bar{3}m$ space group as the parent symmetry. The hypothetical cubic structure of BCO is defined in Appendix A. It was used to decompose the monoclinic $C2/c$ structure in terms of symmetry adapted modes and their irreducible representations (see Appendix B) [21]. In the following analysis, it is sufficient to focus on coupling schemes activated by the largest structural distortions which, from the decomposition result, were antiphase octahedral tilting, $R_4^+(\eta, 0, -\eta)$, and antiferroelectric atomic displacements, $\Lambda_3(0, 0, 0, 0, \epsilon, -\epsilon, -\frac{1}{\sqrt{3}}\epsilon, -\frac{1}{\sqrt{3}}\epsilon, 0, 0, 0, 0, 0, 0, 0, 0)$. The former structural instability is associated with the steric contraction of the perovskite lattice controlled by the Goldschmidt tolerance factor t. The latter instability is associated with the Bi lone pair which often leads to (anti-)ferroelectricity in Bi-containing perovskites [29,30].

The relevant magnetic modes identified above ($F_{x,y,z}$, $G_{x,y,z}$, $L_{x,y,z}$) were also classified in terms of irreducible representations of the cubic parent (see Appendix C). As discussed in Refs. [27,28], the coupling imposed by octahedral tilting can be expressed as a trilinear energy term which, adapted to the present case, reads as $\eta(G_zF_x - G_xF_z)$. This term can be shown to map onto the DM interaction, it is finite only for the type II canting scheme ($G_x \neq 0$, $G_y = 0$, $G_z \neq 0$), and vanishes when the spins are aligned along the b axis in the phase above T_{SR} ($G_x = 0$, $G_y \neq 0$, $G_z = 0$). By contrast, the DM coupling imposed by the Λ_3 structural distortions is described by an energy term of the form $\epsilon(G_yL_z - G_zL_y)$, which is finite in both the high and low temperature magnetic phases. In this case, the weak ferromagnetism arises through an additional higher-order energy term of the form, $(F_xG_x + F_yG_y + F_zG_z)(L_x^2 + L_y^2 + L_z^2)$. This energy term is therefore responsible for weak ferromagnetism above T_{SR}, induced by
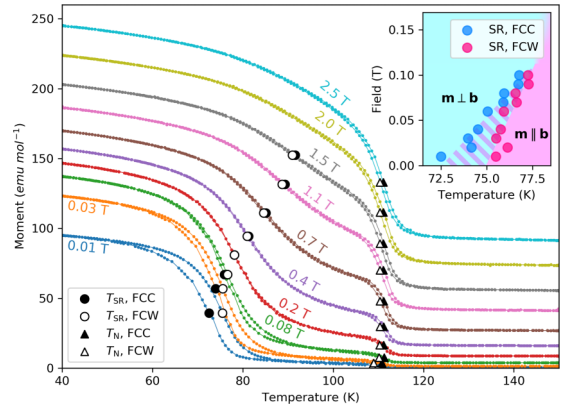

FIG. 7. FCC and FCW magnetization measurements performed in different applied DC fields. Inset: H vs T phase diagram in the vicinity of T_{SR} at low fields, showing the disappearance of thermal hysteresis for fields >1000 Oe. The hatched area represents a region of phase coexistence.

the type I canting scheme. While the type II canting scheme is typical for many AFM perovskites such as REFeO$_3$ orthoferrites and RECrO$_3$ orthochromites, the type I canting scheme represents an original example whereby a net magnetization is induced by structural distortions associated with a lone pair electronic instability.

The above symmetry analysis well explains the observation and relative magnitudes of weak ferromagnetism above and below T_{SR}, but it does not explain the SR transition itself. Both DM anisotropies can be fully satisfied simultaneously if spins are aligned along $\mathbf{c}^*$. However, this moment direction is not observed in any phase and, more crucially, there is no energetic competition leading to SR. The observed SR therefore implies the presence of two further magnetic anisotropies yet to be determined; one potentially weak anisotropy that selects the ground state moment direction from within the planar DM anisotropy, and another stronger anisotropy that competes with the ground state to give moments along $\mathbf{b}$ above T_{SR}. We suggest that these missing anisotropies are an interesting subject for future studies.

Measurements of DC magnetization as a function of temperature under increasing applied DC fields (see Fig. 7) revealed a shift in the SR transition towards higher temperatures, corroborating the ac magnetometry measurement performed by Belik *et al.* [22]. The transition also appears to broaden with increasing field, concomitant with an increase in the magnetization of the intermediate phase ($T_{SR} < T < T_N$), such that it is no longer distinguishable above $H = 2.5$ T. The increase in T_{SR} with increasing field can naturally occur due to the preferential Zeeman coupling of the external field to the larger FM moment in the ground state (type II canting).

The inset of Fig. 7 highlights the field vs temperature behavior of T_{SR} at low fields (thermal gradient maxima of FCC and FCW curves have been used to identify phase boundaries). Below ~ 1000 Oe the SR transition is first order, characterized by a region of phase coexistence between structures transforming as $m\Gamma_1^+$ and $m\Gamma_2^+$. However, as the field is raised above this threshold the hysteresis disappears, consistent with the spin-flop transition evolving into a continuous, second-order transition. We propose that in this regime

the intermediate phase ($T_{SR} < T < T_N$) in the majority of powder grains is characterized by a field-induced admixture of $m\Gamma_1^+$ and $m\Gamma_2^+$ structures permitting a continuous rotation of the weak ferromagnetism, consistent with the increased DC magnetization immediately below T_N.

V. CONCLUSIONS

In summary, we have refined the magnetic structures of BiCrO$_3$ above and below T_{SR}. We confirmed dominant collinear G-type antiferromagnetic order below $T_N = 111$ K, and showed that moments initially lie along the monoclinic b axis, but on cooling through $T_{SR} = 75$ K, undergo a spin reorientation transition to the ground state whereby spins flop into the ac plane along the $[1, 0, \bar{1}]$ direction. These magnetic structures transform by different irreducible representations with respect to their shared paramagnetic parent structure, and thus the transition at T_{SR} is first order; evidenced by large thermal hysteresis in the dc magnetic susceptibility. Using a symmetry-based approach we have shown that weak ferromagnetism above and below T_{SR} likely originates in DM-type interactions associated with antiferroelectric Bi lone-pair ordering and CrO$_6$ octahedral tilting, respectively. While our analysis accurately describes changes in the weak ferromagnetism at T_{SR}, it does not account for the SR transition itself. We, therefore, propose that additional magnetic anisotropies must exist, which are yet to be determined. An applied field was found to destabilize the high temperature magnetic phase, pushing the SR transition to higher temperatures and eventually progressing the transition to a continuous one whereby the order parameter associated with the ground state irrep is finite for all temperatures below T_N.

ACKNOWLEDGMENTS

APPENDIX A: $Pm\bar{3}m$ CUBIC STRUCTURE

Table II details the structure of the $Pm\bar{3}m$ hypothetical cubic perovskite parent unit cell, constructed for the purpose of symmetry analysis.

TABLE II. $Pm\bar{3}m$ unit cell.

Atom	Wyck. Pos.	Site Symm.	Fractional Coord.		
			x	y	z
Bi	1b	$m\bar{3}m$	1/2	1/2	1/2
Cr	1a	$m\bar{3}m$	0	0	0
O	3c	$4/mm.m$	0	1/2	1/2

APPENDIX B: MODE DECOMPOSITION OF 120 K STRUCTURE

Table III presents a mode decomposition of the $C2/c$ structure of BiCrO$_3$ at 120 K with respect to the hypothetical

TABLE III. Displacive mode amplitudes of the 120 K structure with respect to the aristotypical $Pm\bar{3}m$ cubic perovskite parent. Irreps and modes are defined by ISODISTORT (Λ and R irreps correspond to $\mathbf{k} = (-1/4, 1/4, 1/4)$ and $(1/2, 1/2, 1/2)$ respectively). Amplitudes A_s refer to the square root of the sum of the squares of the mode-induced changes within the supercell (the root-summed-squared displacement) while d_{max} refer to the maximum displacement experienced by any atom affected by each mode.

Irrep	Atom	Mode	A_s	d_{max}
Λ_2	O	$Eu(a)$	−0.00286	0.00083
	Bi	$T1u(a)$	0.42766	0.21383
	Cr	$T1u(a)$	0.17920	0.12671
Λ_3	O	$A2u(a)$	0.07920	0.02800
	O	$Eu_1(a)$	0.43971	0.17951
	O	$Eu_2(a)$	−0.35140	0.12424
R_1^+	O	$A2u(a)$	0.00647	0.00187
R_3^+	O	$A2u(a)$	0.02115	0.00863
R_4^+	O	$Eu(a)$	1.20330	0.42543
	Bi	$T1u(a)$	0.11978	0.05989
	Bi	$T1u(b)$	0.09660	0.04830
	O	$Eu(a)$	−0.10150	0.03689
R_5^+	O	$Eu(b)$	−0.05049	0.01785

$Pm\bar{3}m$ cubic parent. Displacive modes Λ_3 and R_4^+ associated with lone-pair-driven antiferroelectric distortions and antiphase octahedral tilts can be clearly identified as those of highest amplitude.

APPENDIX C: MAGNETIC MODES

In Table IV the magnetic $G_{x,y,z}$, $F_{x,y,z}$, $L_{x,y,z}$ modes of BiCrO$_3$ are presented and mapped onto irreducible representations of the $C2/c$ monoclinic unit cell and hypothetical $Pm\bar{3}m$ cubic parent. Fractional coordinates of magnetic chromium atoms in the monoclinic unit cell are detailed in Table V.

TABLE IV. Definition of the magnetic modes by assigning positive or negative spin components for every atom in the monoclinic cell along the direction specified by the mode subscript (see text for Cartesian axes definitions). Columns $C2/c$ Irrep and $Pm\bar{3}m$ Irrep provide the corresponding irreps of the monoclinic and cubic space groups transforming these magnetic modes.

	$C2/c$	$Pm\bar{3}m$	Cr Site							
Mode	Irrep	Irrep	11	12	13	14	21	22	23	24
G_x	$m\Gamma_2^+$									
G_y	$m\Gamma_1^+$	mR_4^+	+	+	+	+	−	−	−	−
G_z	$m\Gamma_2^+$									
F_x	$m\Gamma_2^+$									
F_y	$m\Gamma_1^+$	$m\Gamma_4^+$	+	+	+	+	+	+	+	+
F_z	$m\Gamma_2^+$									
L_x	$m\Gamma_1^+$									
L_y	$m\Gamma_2^+$	$m\Lambda_3$	0	0	0	0	+	−	+	−
L_z	$m\Gamma_1^+$	$m\Lambda_2$								

TABLE V. Cr^{3+} spin sites defined by Wyckoff position, site symmetry and fractional coordinates in $C2/c$ cell.

Mag. Atom	Wyck. Pos.	Site Symm.	Fractional Coord.		
			x	y	z
Cr11			0	$1/4 - \Delta y$	3/4
Cr12	4e	2	0	$3/4 + \Delta y$	1/4
Cr13			1/2	$3/4 - \Delta y$	3/4
Cr14			1/2	$1/4 + \Delta y$	1/4
Cr21			1/4	1/4	1/2
Cr22	4d	$\bar{1}$	1/4	3/4	0
Cr23			3/4	3/4	1/2
Cr24			3/4	1/4	0

[1] C. D. Dashwood, L. S. I. Veiga, Q. Faure, J. G. Vale, D. G. Porter, S. P. Collins, P. Manuel, D. D. Khalyavin, F. Orlandi, R. S. Perry, R. D. Johnson, and D. F. McMorrow, Phys. Rev. B **102**, 180410(R) (2020).

[2] A. V. Kimel, B. A. Ivanov, R. V. Pisarev, P. A. Usachev, A. I. Kirilyuk, and T. H. M. Rasing, Nat. Phys. **5**, 727 (2009).

[3] I. Fita, A. Wisniewski, R. Puzniak, E. E. Zubov, V. Markovich, and G. Gorodetsky, Phys. Rev. B **98**, 094421 (2018).

[4] Y. Yang, R. B. Wilson, J. Gorchon, C.-H. Lambert, S. Salahuddin, and J. Bokor, Sci. Adv. **3**, e1603117 (2017).

[5] N. Locatelli, V. Cros, and J. Grollier, Nat. Mater. **13**, 11 (2014).

[6] A. Sasani, J. Iniguez, and E. Bousquet, Phys. Rev. B **104**, 064431 (2021).

[7] R. L. White, J. Appl. Phys. **40**, 1061 (1969).

[8] X. Ye, J. Zhao, H. Das, D. Sheptyakov, J. Yang, Y. Sakai, H. Hojo, Z. Liu, L. Zhou, L. Cao, T. Nishikubo, S. Wakazaki, C. Dong, X. Wang, Z. Hu, H. J. Lin, C. T. Chen, C. Sahle, A. Efiminko, H. Cao *et al.*, Nat. Commun. **12**, 1 (2021).

[9] A. M. Vibhakar, D. D. Khalyavin, P. Manuel, J. Liu, A. A. Belik, and R. D. Johnson, Phys. Rev. Lett. **124**, 127201 (2020).

[10] C. Darie, C. Goujon, M. Bacia, H. Klein, P. Toulemonde, P. Bordet, and E. Suard, Solid State Sci. **12**, 660 (2010).

[11] S. Niitaka, M. Azuma, M. Takano, E. Nishibori, M. Takata, and M. Sakata, Solid State Ionics **172**, 557 (2004).

[12] A. A. Belik, S. Iikubo, K. Kodama, N. Igawa, S. Shamoto, and E. Takayama-Muromachi, Chem. Mater. **20**, 3765 (2008).

[13] C. V. Colin, A. G. Pérez, P. Bordet, C. Goujon, and C. Darie, Phys. Rev. B **85**, 224103 (2012).

[14] J. P. Cardoso, D. Delmonte, E. Gilioli, E. L. Fertman, A. V. Fedorchenko, V. V. Shvartsman, V. Paukšta, R. Grigalaitis, J. R. Banys, D. D. Khalyavin, J. M. Vieira, and A. N. Salak, Inorg. Chem. **59**, 8727 (2020).

[15] B. S. Araújo, A. M. Arévalo-López, C. C. Santos, J. P. Attfield, C. W. A. Paschoal, and A. P. Ayala, J. Appl. Phys. **127**, 114102 (2020).

[16] N. A. Hill, P. Bättig, and C. Daul, J. Phys. Chem. B **106**, 3383 (2002).

[17] C. Goujon, C. Darie, M. Bacia, H. Klein, L. Ortega, and P. Bordet, J. Phys.: Conf. Ser. **121**, 022009 (2008).

[18] L. C. Chapon, P. Manuel, P. G. Radaelli, C. Benson, L. Perrott, S. Ansell, N. J. Rhodes, D. Raspino, D. Duxbury, E. Spill, and J. Norris, Neutron News **22**, 22 (2011).

[19] J. Rodríguez-Carvajal, Physica B **192**, 55 (1993).

[20] H. T. Stokes, D. M. Hatch, and B. J. Campbell, ISOTROPY Software Suite, https://iso.byu.edu.

[21] B. J. Campbell, H. T. Stokes, D. E. Tanner, and D. M. Hatch, J. Appl. Crystallogr. **39**, 607 (2006).

[22] A. A. Belik, N. Tsujii, H. Suzuki, and E. Takayama-Muromachi, Inorg. Chem. **46**, 8746 (2007).

[23] See Supplemental Material at http://link.aps.org/supplemental/10.1103/PhysRevB.106.024416 for .mcif files of the magnetic structures and ISOVIZ files of the mode decomposition of the crystal structure.

[24] F. Bloch, Z. Phys. **61**, 206 (1930).

[25] S. Blundell, *Magnetism in Condensed Matter*, Oxford Master Series in Condensed Matter Physics (Oxford University Press, Oxford, 2001).

[26] I. Dzyaloshinsky, J. Phys. Chem. Solids **4**, 241 (1958).

[27] D. D. Khalyavin, A. N. Salak, N. M. Olekhnovich, A. V. Pushkarev, Y. V. Radyush, P. Manuel, I. P. Raevski, M. L. Zheludkevich, and M. G. S. Ferreira, Phys. Rev. B **89**, 174414 (2014).

[28] D. D. Khalyavin, A. N. Salak, P. Manuel, N. M. Olekhnovich, A. V. Pushkarev, Y. V. Radysh, A. V. Fedorchenko, E. L. Fertman, V. A. Desnenko, and M. G. S. Ferreira, Z. Kristallogr. Cryst. Mater. **230**, 767 (2015).

[29] R. Seshadri and N. A. Hill, Chem. Mater. **13**, 2892 (2001).

[30] J. B. Neaton, C. Ederer, U. V. Waghmare, N. A. Spaldin, and K. M. Rabe, Phys. Rev. B **71**, 014113 (2005).